# A behavioural framework for fibre reinforced gravel

Olufemi Ajayi[1*], Louis Le Pen[1], Antonis Zervos[1] and William Powrie[1]

31 May 2016

| | |
|---|---|
| Word count | - 5,013 |
| Number of tables | - 4 |
| Number of figures | - 20 |

doi: 10.1680/jgeot.16.P.023

[1]Faculty of Engineering and the Environment, University of Southampton, Southampton, SO17 1BJ, United Kingdom.

[*]Corresponding author - o.o.ajayi@soton.ac.uk

## Abstract

The mechanical behaviour of granular materials is known to be influenced by the addition of fibres. However, most previous research has been carried out on materials with relatively small grains (sands), and its application to larger grains is not well documented. This paper reports an investigation into the mechanical behaviour of a fibre reinforced granular material having a relatively large grain size corresponding to 1/3rd and 1/5th scaled railway ballast. The investigation was carried out by means of triaxial tests incorporating a full-field, image-based deformation measurement technique; this enabled detailed observations to be made of each triaxial test specimen during shearing. The test data demonstrate the benefits of random fibre reinforcement for aggregates having a relatively large grain size. Analysis taking into account the effect of fibre tension on the effective stresses experienced by the granular skeleton provides new insights into the mechanisms of reinforcement in larger sized granular materials.



**Keywords:** fibre reinforcements, digital image correlation, granular materials, railway ballast

# 1 Introduction

Ballast is a primary component of a traditional railway track system. It resists and distributes the vertical, lateral and longitudinal forces applied to the sleepers from trains via the rails. The mechanical behaviour of railway ballast, like granular soils, can be improved by the addition of geosynthetics. For example, geogrids improve the performance of a ballast bed by restricting the lateral movement of ballast grains (McDowell et al., 2006), reducing both lateral spread and vertical settlement (Indraratna et al., 2010; Chen et al., 2012). A drawback of geogrids in ballast is the resulting restriction on the future depth of tamping, which must be limited to avoid destroying the geogrids. The addition of randomly placed (although not necessarily randomly oriented) synthetic strips (referred to hereafter as fibres) could provide an alternative method of ballast reinforcement that is less susceptible to damage by tamping operations.

It is known that the introduction of randomly placed fibres can significantly improve the strength and ductility of sands (e.g. Michalowski and Cermak, 2002; Lirer et al., 2011; Diambra et al., 2013). Results from a well-graded gravel with grain sizes in the range 0.2 – 10 mm were reported by Lirer et al. (2011) and initial tests on scaled and full size railway ballast materials have shown some promise (Ajayi, 2014; Abadi, 2015), but research on fibre reinforced granular materials has to date focused mainly on fine to medium sands. In general, the effectiveness of fibre reinforcements in sands is influenced by: (1) *fibre properties* including geometry (e.g. length, diameter, aspect ratio), elastic modulus and tensile strength; (2) *soil characteristics* including grain size, shape and gradation; (3) the *characteristics of the mixture* including (relative) density, fibre content, fibre/grain relative dimensions and fibre orientation; and (4) *external controls* such as the confining or normal effective stress (Michalowski and Zhao, 1996; Diambra et al., 2013; Li and Zornberg, 2013; Ajayi et al., 2014). However, neither the effect of fibre (strip) reinforcements nor the underlying micromechanics of grain-fibre interaction have been fully investigated for larger grain size aggregates. While these might be expected to be similar to those for finer grained materials provided that the fibre dimensions and content are appropriately scaled, such scaling laws have not yet been established.

This paper reports an investigation, based on a series of triaxial tests, into the mechanical behaviour of two fibre reinforced granular materials having a relatively large grain size, corresponding to $^1/_3$ and $^1/_5$ scale railway ballast). Monitoring using a full-field, image-based deformation measurement technique enabled detailed observations to be made of the development of deformations throughout each triaxial test specimen during shearing. An analysis that takes account of the effect of tension in the fibres in increasing the effective stress experienced by the granular matrix is presented, and together with the experimental results is used to gain some new insights into the mechanisms of fibre-grain interaction that lead to the improved mechanical behaviour of the composite material.

## 2 Materials and methods

### 2.1 Materials

Two parallel gradations of crushed granite from the same quarry (having $D_{50}$ = 8 mm and 14 mm, $^1/_5$ and $^1/_3$ of the size of typical railway ballast), were used in this work (Figure 1). Le Pen et al. (2013) demonstrated that, although measurable variations in grain shape occur over a range of sieve intervals, these differences are relatively slight and do not militate against the use of scaled material in investigating the mechanical behaviour of a coarser aggregate. This agrees with the findings of Sevi (2008). Physical model tests involving scaled ballast (which hereafter may be abbreviated to SB) have been used to investigate the development of plastic deformation under cyclic (Sevi et al., 2009) and moving wheel loads (Ishikawa et al., 2011); and how the dimensions of the ballast shoulder contribute to the resistance of a railway sleeper to lateral movement (Koike et al., 2014; Le Pen et al., 2014).

Tape-like polyethylene fibres (Figure 2), cut to size from lightly-textured damp proof course (DPC) material, were used in this work. The textured surface of the fibres was relatively smooth (with a roughness of about 0.1mm), hence was not considered explicitly in the interpretation of the laboratory test results. Their typical mechanical properties are summarised in Table 1. The effect of changing the fibre content was investigated but not fibre length and width, which were kept constant relative to the grain size in the tests reported in this paper.

### 2.2 Phase relations and initial specimen density

In interpreting the mechanical behaviour of fibre reinforced granular materials, the volume of fibres is sometimes considered to be part of the volume of solids and sometimes part of the volume of voids. In this paper, a three phase system proposed by Ajayi et al. (2014) in which the voids (air), grains and fibres are treated separately is adopted. Relations between the phases are defined as

*Void ratio* ($e$): the ratio of the volume of voids ($V_v$) to the volume of the grains ("solids"), ($V_s$)

$$e = \frac{V_v}{V_s} \tag{1}$$

*Volumetric fibre ratio* ($V_{fr}$): the ratio of the volume of fibres ($V_f$) to the volume of solids ($V_s$)

$$V_{fr} = \frac{V_f}{V_s} \tag{2}$$

*Specific volume* ($v$): the ratio of the total volume (fibres + solids + voids, $V_T = V_s + V_f + V_v$) to the volume of solids ($V_s$)

$$v = \frac{V_s + V_f + V_v}{V_s} = 1 + e + V_{fr} \quad (3)$$

These definitions have the advantage of considering the fibres independently of both the solids and the voids, while taking $V_s$ as the common denominator. They also facilitate an interpretation of the observed behaviour based on the void ratio of the granular matrix alone, as discussed later.

There is no standard way of preparing specimens of fibre reinforced granular materials to a given density. Thus a variety of methods have been developed (e.g. Michalowski and Zhao, 1996; Ibraim and Fourmont, 2007), albeit for fibre reinforced sand rather than larger and more uniformly-graded aggregates like scaled ballast.

In the research reported in this paper, fibre reinforced scaled ballast was prepared by hand-mixing known masses of fibres and scaled ballast in a plastic container to achieve a mixture comprising randomly distributed fibres and scaled ballast. The mixed material was then compacted in three layers into a cylindrical mould 150 mm in diameter and 246 mm high. Tests showed that twenty (20) blows from a standard Proctor rammer of mass 2.5 kg produced a density similar to that using the vibration method of compaction described later. This was taken as the realistic maximum achievable density. To prevent grain breakage by direct impact from the rammer, a circular piece of laminated wood padded with rubber was placed on top of the uppermost layer during compaction.

The resulting mixture showed a reasonably random distribution of fibre location. The orientation of the fibres was observed to be mostly sub-horizontal; likely an inevitable consequence of the placement/compaction procedure and the size of the fibres and granular material used. This is considered satisfactory, because (1) the compaction procedure is not too different from a typical field process, (2) repeatability between tests on different specimens was good, and (3) the preferential sub-horizontal orientation of the fibres was similar to that reported by Diambra et al. (2008) of generally between ±30° of horizontal. Minimum density specimens were prepared by carefully placing the material piecewise by hand into the cylindrical mould, to achieve as open a structure as possible.

Figure 3 shows that the maximum and minimum void ratios ($e_{max}$ and $e_{min}$) achievable with a given compactive effort increase gradually with increasing $V_{fr}$. In other words, the addition of fibres interferes with the packing of the grains. This was also observed by Michalowski and Zhao (1996), Ibraim and Fourmont (2007), who attributed it to the greater resistance to compaction in the presence of the fibres, and by Dos Santos et al. (2010).

A consequence of the data presented in Figure 3 is that the addition of fibres leads to the possibility that the density index (relative density) of the specimen $I_D$,

$$I_D = \frac{e_{max} - e}{e_{max} - e_{min}} \quad (4)$$

where $e_{max}$ and $e_{min}$ are the maximum and minimum void ratios for the unreinforced scaled ballast, could be negative.

## 2.3 Fibre dimensions

The fibre length, $L_f$, and the fibre width, $W_f$, are quantified relative to the mean grain size of the scaled ballast, $D_{50}$, in terms of the normalized dimensions, $L_N$ and $W_N$, where

$$L_N = \frac{L_f}{D_{50}} \quad (5)$$

$$W_N = \frac{W_f}{D_{50}} \quad (6)$$

The fibre thickness was kept constant; it is assumed that individual fibres remained flexible with negligible bending stiffness. The fibre dimensions and contents used are given in Table 2.

## 2.4 Image-based local deformation measurement

Using digital cameras to monitor the deformation of soils can provide effectively continuous information across the full field of deformation. Digital image analysis has been used to determine deformations of soil models in a geotechnical centrifuge (e.g. White et al., 2003); and to measure local strains and study strain localisation in laboratory element tests on plane strain or circular cylindrical specimens tested outside a triaxial cell (e.g. Liang et al., 1997; Macari et al., 1997; Alshibli and Al-Hamdan, 2001; Rechenmacher and Finno, 2004; Gachet et al., 2007; Sevi et al., 2009). In the current study, the image-based deformation measurement method developed by Bhandari et al. (2012), Triax-DIC, which uses ray-tracing to account for refraction through the triaxial cell wall and confining fluid, was used.

Two digital cameras (SONY DSC-R1 Cyber shot 10 mega pixel) were attached to cantilever arms fixed to the base of the triaxial apparatus so that they would remain in the same position relative to the base of the specimen during shear (Figure 4). The cameras were placed along cell radii at an angular separation of ~120° on plan, with their optical axes at the mid-height of the specimen. Although this arrangement does not enable imaging of the whole circumference of the specimen, any tendency for localisation (which manifests on diametrically opposite sides) will be visible on at least one of the cameras. Images of the deforming specimen were captured at intervals of 0.25 % axial strain. An artificial texture for image correlation was produced by spraying quick-drying enamel paint onto the membrane. The triaxial apparatus comprising the cell, two digital cameras, a light source and reflector is shown in Figure 4. It is described in detail by Bhandari et al. (2012) and summarised in Table 3.

Measurement points were on a 15 mm square grid, covering an area of 135 mm × 195 mm (more than half the height of the specimen), centred at mid-height (Figure 5). Having determined the displacement components in both the $x$ (circumferential) and $y$ (vertical) directions at each measurement point, the region was divided into quadrilateral elements and bilinear interpolation was used to determine the principal and maximum shear strains for each element as described by Bhandari et al. (2012).

## 2.5 Triaxial test apparatus and procedure

Strain-controlled triaxial tests were carried out on 150 mm diameter × 300 mm high specimens. Global axial displacement was measured using a displacement transducer (LVDT) located on top of the triaxial cell, and the axial force using an internal load cell. Local instrumentation attached to the specimen was not used, owing to the erratic nature of measurements resulting from unpredictable movements of the relatively large grains. Also, the strains in typical railway ballast tested to failure fall within the range of reliable measurement of a global axial displacement transducer (Atkinson, 2000). A transducer attached to the cell pressure inlet measured the cell pressure being applied to the specimen. The triaxial tests were carried out on dry specimens internally open to the atmosphere, i.e. without the application of back pressure. Specimen volume change was measured by the cell pressure controller. Aingaran (2014) demonstrates that the maximum potential error in the volumetric strain associated with cell volume changes over a 24 hour period using this set up is less than 0.1 %, and Figure 6 shows that the results from tests on dry and saturated unreinforced $^1/_3$ SB, in which specimen volume changes were determined from the cell and pore pressure controllers respectively, are the same. Pressures and volumes were measured to a resolution of 0.1 kPa and 1 mm$^3$ respectively.

The fibre reinforced specimens used in the triaxial tests reported in this paper were prepared using the same compactive effort, giving a void ratio that varied with the fibre content. For comparative purposes, loose and dense unreinforced specimens of both scaled ballasts were also tested.

Dense specimens were prepared by placing known quantities of previously hand-mixed fibres and grains within a split cell mould lined with a rubber membrane, followed by vibratory compaction under a 5 kg surcharge. The loose unreinforced specimens were prepared by placing a long narrow tube (diameter 100 mm), open at both ends, upright in a split mould on the triaxial pedestal. Sufficient scaled ballast to fill the mould was then placed into the tube and the tube was slowly lifted, allowing the grains to descend gently into the mould. The range of void ratios achieved allows comparisons to be made between reinforced and unreinforced specimens of the same scale on the basis of having the same initial void ratio (Eq. 1) or relative density index (Eq. 4) (Figure 7). The triaxial tests were carried out at a cell pressure of 30 kPa, which is at the upper end of the likely range of in situ lateral stresses in railway ballast (e.g. Indraratna et al., 2010; Sevi and Ge, 2012) and was kept constant during shear. The initial condition of each specimen is summarised in Table 2.

# 3 Triaxial test results and analysis

## 3.1 Stress-strain and volumetric behaviour

Figure 8 shows graphs of deviator stress, $q$ (defined in the conventional way as $q = \sigma_a - \sigma_r$) and volumetric strain $\varepsilon_{vol}$ against axial strain $\varepsilon_a$ for triaxial tests on unreinforced $^1/_3$ and $^1/_5$ SB at different initial relative density and void ratio. All of the specimens exhibited initial contraction and subsequent dilation, with (as expected) the degree of dilation increasing with initial density.

Figure 9 shows the corresponding data for specimens of $^1/_3$ and $^1/_5$ SB with increasing amounts of fibre reinforcement ($V_{fr}$). In both materials, increasing $V_{fr}$ delayed the occurrence and increased the magnitude of the peak deviator stress, decreased the initial stiffness, improved ductility and suppressed dilation. This type of behaviour was reported by Michalowski and Cermak (2003), Heineck et al. (2005) and Diambra et al. (2010) for reinforced and unreinforced specimens of sand having the same initial void ratio.

The reduced dilatant volumetric strain of the reinforced specimens is consistent with their looser packing (higher $e_o$ in Table 2), and the reduction in dilation is reflected in a general increase in ductility. However, the increase in peak deviator stress $q$ is not consistent with either the reduction in dilation or the increase in ductility, according to established soil mechanics principles. Thus the change in behaviour cannot be attributed solely to the change in the initial void ratio, and a deeper explanation is required.

Furthermore, Table 2 shows that the initial void ratio, $e_o$, for the specimens with $V_{fr}$ = 1.6% is close to that for the corresponding medium or dense unreinforced specimen (for the $^1/_5$ SB, $e_o$ = 0.83 for both $V_{fr}$ = 1.6% and the medium dense unreinforced specimen; while for the $^1/_3$ SB, $e_o$ = 0.79 for $V_{fr}$ = 1.6% and $e_o$ = 0.76 for the dense unreinforced specimen). For the specimens with $V_{fr}$ = 3.2 %, $e_o$ is in both cases close to that for the corresponding loose unreinforced specimen (for the $^1/_5$ SB, $e_o$ = 0.88 for $V_{fr}$ = 3.2% and $e_o$ = 0.89 for the loose unreinforced specimen; while for the $^1/_3$ SB, $e_o$ = 0.91 for $V_{fr}$ = 3.2% and $e_o$ = 0.87 for the loose unreinforced specimen). Yet Figure 10 shows that the mechanical behaviour of specimens having the same $e_o$ but different $V_{fr}$ is very different. (The discrepancies in the initial void ratios just lie within the range of precision in typical measurements of $e_o$, of ± 0.02 or 8 % of the void ratio range, $e_{max} - e_{min}$, of the unreinforced material; thus for the purpose of comparison can reasonably be neglected).

## 3.2 Stress-dilatancy

Figures 11 and 12 show relationships between stress ratio, $\eta = q/p$, and the rate of dilation, $d$, (Eq. 5) for unreinforced and reinforced specimens of $^1/_3$ and $^1/_5$ SB, respectively. $d$ is defined as

$$d = -\left(\frac{\delta\varepsilon_{vol}}{\delta\varepsilon_{\gamma}}\right) \tag{7}$$

where $\delta\varepsilon_{vol}$ is the volumetric strain increment and $\delta\varepsilon_{\gamma}$ is the triaxial shear strain increment, $\delta\varepsilon_{\gamma} = 2/3(\delta\varepsilon_{axial} + \delta\varepsilon_{radial})$. In triaxial tests with $u = 0$, the values of $q$ and $p$ calculated as $q = \sigma_a - \sigma_r$ and $p = (\sigma_a + 2\sigma_r)/3$ would conventionally be viewed as effective stresses.

As would be expected, for both $^1/_3$ and $^1/_5$ SB, $d_{max}$ is greater for the dense unreinforced specimens than for the medium and loose unreinforced specimens, while all unreinforced specimens of the same material exhibited the same stress ratio at zero dilation. This is not the case for the fibre reinforced specimens, for which the stress ratio at zero dilation and the slope of the stress-dilatancy relationship at higher rates of dilation are significantly different. Similar results have been reported by, for example, Michalowski and Cermak (2003) and Dos Santos et al. (2010).

The fact that fibre reinforced materials appear to behave differently from their unreinforced counterparts is generally attributed to the mobilisation of tensile forces in the fibres. However, previous researchers have interpreted the effect in two different ways: (1) the higher apparent stress ratio at zero dilation indicates an increase in the underlying fundamental steady or critical state strength (e.g. Dos Santos et al., 2010); and (2) the critical state stress ratio of the granular matrix at zero dilation does not change, but the stretched fibres increase the lateral stresses in the granular matrix, permitting a higher axial stress so that the apparent stress ratio increases (e.g. Diambra et al., 2013). Depending on the fibre orientation relative to the applied stresses, the fibre tension may also contribute to carrying the shear stress directly (Jewell and Wroth, 1987). The first approach has pragmatic practical merit, while the second offers a more fundamental insight into the mechanics of the interactions between the grains and the fibre reinforcements.

Diambra et al. (2013) developed a constitutive model for fibre reinforced sands based on the principle of the superposition of the stress and strain states of the sand matrix and fibres. The sand matrix was assumed to obey its own constitutive laws, with the fibres considered as discrete forces with defined orientations. Here, we develop the model proposed by Jewell and Wroth (1987) in which the tension generated in the fibres as the material strains "*increases the normal effective stress….., allowing additional frictional shearing resistance to be mobilised*". In their analysis of direct shear tests, Jewell and Wroth (1987) also allowed for a reduction in the shear stress carried by the granular matrix as a result of the component of the fibre tension tangential to the shear plane. In the current triaxial tests, the fibres are oriented predominantly along the direction of the applied minor principal stress, hence this latter possibility is not considered here. Our analysis is based on the hypothesis that tension in the fibres creates an additional stress on the granular skeleton, which can be added to the total stress (minus any pore water pressure) to give the effective stress experienced by the granular skeleton. This can then be treated in the usual way within a conventional soil mechanics framework.

### 3.3 Contribution of fibre tension to the effective stress experienced by the granular skeleton

The following analysis is deliberately simple, and is intended to illustrate conceptually how the fibres make the stresses experienced by the granular matrix different from those applied at the boundary, for the current application of the triaxial test.

Consider an element of reinforced gravel containing a volume of grains $v_g$, having a void ratio $e$ and a volumetric fibre ratio $V_{fr}$. Each fibre has Young's modulus $E_f$; the total cross sectional area of fibre per unit volume of grains is $A_f$; and the average orientation of the fibres is at an angle $\beta$ to the horizontal.

Following placement of the fibres in a stress-free state, the reinforced gravel element has been subjected to a lateral tensile strain $\varepsilon_r$. The maximum horizontal strain, $\varepsilon_{fmax}$, in each fibre will be less than $\varepsilon_r$ because (i) the fibre orientation is not exactly horizontal, (ii) tension will not develop uniformly along the whole fibre owing to the need for an "anchor length" at each end, and (iii) relative slip between the fibre and the surrounding grains where the frictional strength of the grain-fibre interface is fully mobilised. The average horizontal (radial) force, $F$, in each fibre is then $\varepsilon_{fmax} \times E_f \times A_f \times \cos\beta$. The fibre orientation $\beta$, interface slip and the fibre "anchor lengths", may be accounted for using a fibre/grain interaction factor, $\alpha$, such that the average horizontal force in each fibre is $\alpha \times \varepsilon_r \times E_f \times A_f$, where $\alpha \leq 1$. If the vertical area ratios of the phases in the reinforced scaled ballast are the same as the volumetric ratios,

$$A_f = \frac{V_f}{V_g} \cdot A_g = V_{fr} \cdot A_g \tag{8}$$

where $A_g$ is the area of grains; and the fibre force acts over a total area, $A$, of $A_g \times (1 + e + V_{fr})$.

Hence the enhancement to the effective horizontal stress experienced by the granular skeleton at a radial strain $\varepsilon_r$ is

$$\frac{F}{A} = \sigma'_f = \frac{\alpha \cdot \varepsilon_r \cdot E_f \cdot V_{fr}}{\left(1 + e + V_{fr}\right)} \tag{9}$$

This additional effective stress only acts in the horizontal direction (Figure 13) because (i) the axial stress is compressive (and is it assumed that the fibres have no stiffness in compression) and (ii) the orientation of the fibres is substantially horizontal.

The fibre/grain interaction factor, $\alpha$, will in general vary with strain and has been assumed to take the form shown in Eq.10.

$$\alpha = A_\alpha \left|\varepsilon_r\right|^{-B_\alpha} \tag{10}$$

where $A_\alpha$ and $B_\alpha$ are constants for a given combination of granular material, fibre type, fibre geometry and fibre content. The fibre/grain interaction factor α must lie in the range $0 \leq \alpha \leq 1$. The values of $A_\alpha$ and $B_\alpha$ were determined by curve-fitting (see below), and fall in the ranges $0.220 \leq A_\alpha \leq 0.147$, and $0.4 \leq B_\alpha \leq 0.6$.

The corrected radial stress on the granular skeleton, denoted $\sigma''_3$, is then

$$\sigma''_3 = \sigma'_3 + \sigma'_f \tag{11}$$

As already explained, the axial stress is unaffected.

The corrected deviator stress, $q''$, and corrected mean effective stress, $p''$, then become

$$q'' = q - \sigma'_f \tag{12}$$

$$p'' = \frac{1}{3}\left(\sigma''_1 + 2\sigma''_3\right) = p' + \frac{2}{3}\sigma'_f \tag{13}$$

The stress correction parameters are shown in Table 4 and a typical evolution of the additional effective lateral stress, $\sigma'_f$, in Figure 14. The resulting stress-dilatancy plots are shown in Figure 15.

In the initial stages (corresponding to sample compression), the correction makes little difference to the stress-dilatancy plots until the rate of compression starts to decrease. At $d = 0$ and subsequent positive rates of dilation, the corrected stress ratio is the same for the reinforced specimens as for the unreinforced specimens. (This was the basis on which the values of the parameters $A_\alpha$ and $B_\alpha$ were determined).

Figure 16 shows that the corrected data of maximum mobilised stress ratio, $\eta_{max}$, against the rate of dilation at $\eta_{max}$, lie on the same trend line for all specimens (reinforced and unreinforced) of both scaled ballasts, giving a close fit to the Cam clay stress-dilatancy relationship $\eta = M + d$ (Schofield and Wroth, 1968).

### 3.4 Corrected stress-strain behaviour

Figures 17 and 18 compare graphs of corrected stress ratio $\eta'' = q''/p''$ against axial strain for reinforced and unreinforced specimens of $^1/_3$ and $^1/_5$ SB respectively. For comparative purposes, the uncorrected stress ratios for the reinforced specimens are also shown.

In each case, the corrected curves are located as expected in relation to those for the corresponding unreinforced material. In Figure 17(a), the corrected stress-strain curve for the reinforced $^1/_3$ SB with $V_{fr}$ = 1.6% ($e_o$ = 0.79) lies between the curves for the dense ($e_o$ = 0.76) and the loose ($e_o$ = 0.87) unreinforced material, whereas the uncorrected curve lay above that for the dense unreinforced gravel. In Figure 17(b), the corrected stress-strain curve for the reinforced material with $V_{fr}$ = 3.2% ($e_o$ = 0.91) lies below the curve for the

loose unreinforced material having $e_o$ = 0.87, whereas the uncorrected stress-strain curve rose above that for the dense unreinforced gravel having $e_o$ = 0.76.

Similarly in Figure 18(a), the corrected stress-strain curve for the reinforced $^1/_5$ SB with $V_{fr}$ = 1.6% ($e_o$ = 0.83) lies between the curves for the dense ($e_o$ = 0.74) and the loose ($e_o$ = 0.89) unreinforced material, whereas the uncorrected stress-strain curve lay above that for the dense unreinforced gravel. In Figure 18(b), the corrected stress-strain curve for the reinforced material with $V_{fr}$ = 3.2% ($e_o$ = 0.97) lies below the curve for the loose unreinforced material ($e_o$ = 0.89), whereas the uncorrected stress-strain curve rose above that for the dense unreinforced gravel ($e_o$ = 0.74).

Figures 17 and 18 show that the stress correction brings the stress-strain curves into line with what would be expected on the basis of their granular void ratios, relative to the maximum and minimum void ratios achievable for the unreinforced granular matrix.

## 4 Full field deformation measurements

Images of the $^1/_5$ SB triaxial specimens acquired during the shear stage of each test were analysed to assess the developing deformation patterns. For brevity, only selected typical images from one camera are presented, analysed from a global axial strain of 0.25 % onward.

Figure 19 shows displacement vectors with superimposed contours of constant displacement magnitude. The horizontal axis of each plot represents distance around the circumference of the specimen and the vertical axis the specimen height (both in mm). In general, displacements at a given axial strain become more vertical (with a decreasingly significant radial component) as the fibre content increases. This might be attributed to the higher initial void ratio, but may also be a result of the increased lateral effective stress that results from the development of tensions in the fibres. However, it is certainly consistent with reduced dilation.

Figure 20 shows trend lines (smoothing splines fitted to the raw data) illustrating the relative frequency of local maximum (direction-dependent) shear strain at each point at a global cumulative axial strain of 10 %, for specimens of $^1/_5$ SB having different fibre contents $V_{fr}$ and broadly similar relative density index $I_D$ (range 0.96 to 0.99). The effect of increasing $V_{fr}$ in reducing both the average magnitude of the shear strain (indicating reduced dilation) and the range of shear strain (indicating more uniform specimen deformation) is clear.

Strain localisation, not readily discernible by the naked eye until a clear shear band develops (Alshibli et al., 2003; Rechenmacher, 2006), is evidenced by the relatively non-uniform patterns of displacement vectors and contours in the unreinforced (Figure 19a - c) and the lightly reinforced specimens (Figure 19d and e). The specimen having $V_{fr}$ = 6.5 % did not exhibit localisation, as evidenced by the near-parallel displacement contour lines and more uniform displacement pattern (Figure 19f).

Strain localisation is associated with the development of micro voids and the onset of dilation (e.g. Desrues et al., 1996; Hall et al., 2010) as individual grains rotate and displace, leading to the disruption of the fabric of the material (Cresswell and Powrie, 2004). This implies that the addition of sufficient fibres to scaled ballast resists the disruptive processes of grain rotation and displacement that lead to localised deformation during the early stages of a shear test.

In summary, it is suggested that the addition of fibres improves the mechanical properties of large grained geomaterials by

i. initially restricting grain movement, and at larger strains developing tensions that increase the lateral effective stress on the granular skeleton, so that at a given vertical strain, the lateral strain is reduced compared with the corresponding unreinforced material.
ii. promoting a more uniform distribution of deformations and strains during triaxial shear, compared with the corresponding unreinforced material. If sufficient fibres are added (in these tests, a volume fraction $V_{fr}$ of between 3.2% and 6.5%), early strain localisation is inhibited.

# 5 Conclusions

1. Results have been presented from triaxial tests carried out to investigate the effect of adding randomly-distributed fibre reinforcement to gravels representing $^1/_3$ and $^1/_5$ scale railway ballast. The results have been interpreted using a conceptual model in which an additional lateral effective stress is assumed to act on the granular skeleton in proportion to the volumetric fibre ratio, the Young's modulus of the fibres and dependent on the lateral strain. This approach brings the stress-strain and stress-dilatancy relationships of the reinforced materials into line with the expectations of established soil mechanics principles. If the additional effective stress is not taken into account, the results of tests appear anomalous with loose specimens exhibiting higher apparent stress ratios at lower rates of dilation than dense specimens.

2. The addition of small amounts of appropriately sized randomly-distributed fibres to gravels corresponding to $^1/_5$ and $^1/_3$ scale railway ballast enables the granular matrix to take up a looser state than would be possible for the unreinforced material. While this leads to a slight reduction in the initial shear and volumetric stiffnesses, it increases the external load carrying capacity of the material (because the effect of the reinforcement in increasing the effective stress on the granular skeleton is internal), reduces the propensity of the material to dilate and improves ductility.

3. In triaxial tests, the addition of fibres results in a reduced lateral strain and a more uniform distribution of deformations and strains within the specimen during shear, compared with the

corresponding unreinforced gravel. If sufficient fibres are added (a minimum volume fraction $V_{fr}$ of between 3.2 % and 6.5 % is suggested), early strain localisation is prevented.

4. It is suggested that the addition of fibres to scaled ballast restricts the disruptive processes of grain rotation and displacement that lead to localised deformation during the early stages of shear. At larger displacements the fibres develop tension, which increases the effective lateral stress and hence also helps to resist dilation.

## Acknowledgements

This research was supported by the UK Engineering and Physical Sciences Research Council (EPSRC) through the "Railway Track for the 21st Century - *TRACK21"* Programme Grant (EP/H044949). The first author further acknowledges the support of the University of Southampton.

## References

Abadi, T. (2015). *Effect of Sleeper and Ballast Interventions on Performance.* PhD. Thesis, University of Southampton.

Aingaran, S. (2014). *Experimental investigation of static and cyclic behaviour of scaled railway ballast and the effect of stress reversal.* PhD. Thesis, University of Southampton.

Ajayi, O. (2014). *The effect of fibre reinforcements on the mechanical behaviour of railway ballast.* PhD. Thesis, University of Southampton.

Ajayi, O., Le Pen, L. M., Zervos, A. & Powrie, W. (2014). Effects of random fibre reinforcement on the density of granular materials. *In:* SOGA, K., KUMAR, K., BISCONTIN, G. & KUO, M., eds. Geomechanics from Micro to Macro, 1 - 3 September 2014 University of Cambridge, Cambridge UK. CRC Press/Balkema, p. 1363-1367.

Alshibli, K., Batiste, S. & Sture, S. (2003). Strain Localization in Sand: Plane Strain versus Triaxial Compression. *Journal of Geotechnical and Geoenvironmental Engineering, ASCE,* 129(6), 483-494.

Alshibli, K. A. & Al-Hamdan, M. Z. (2001). Estimating volume change of triaxial soil specimens from planar images. *Computer-Aided Civil and Infrastructure Engineering,* 16(6), 415-421.

Atkinson, J. H. (2000). Non-linear soil stiffness in routine design. *Géotechnique,* 50(5), 487-508.

Bhandari, A. R., Powrie, W. & Harkness, R. M. (2012). A Digital Image-Based Deformation Measurement System for Triaxial Tests. *Geotechnical Testing Journal, ASTM,* 35(2), 209-226.

Bouguet, J.-Y. (2008). *Camera Calibration Toolbox for Matlab* [Online]. Available: http://www.vision.caltech.edu/bouguetj/calib_doc/index.html [Accessed 12/02/2014.

Chen, C., Mcdowell, G. R. & Thom, N. H. (2012). Discrete element modelling of cyclic loads of geogrid-reinforced ballast under confined and unconfined conditions. *Geotextiles and Geomembranes,* 35(0), 76-86.

Cresswell, A. & Powrie, W. (2004). Triaxial tests on an unbonded locked sand. *Geotechnique,* 54(2), 107-115.

Desrues, J., Chambon, R., Mokni, M. & Mazerolle, F. (1996). Void ratio evolution inside shear bands in triaxial sand specimens studied by computed tomography. *Geotechnique,* 46(3), 529-546.

Diambra, A., Ibraim, E., Russell, A. R. & Wood, D. M. (2013). Fibre reinforced sands: from experiments to modelling and beyond. *International Journal for Numerical and Analytical Methods in Geomechanics,* 37(15), 2427-2455.

Diambra, A., Ibraim, E., Wood, D. M., Bennanni, Y. & Russell, A. R. (2008). Effect of sample preparation on the behaviour of fibre reinforced sands. Proceedings of the 4th International Symposium on Deformation Characteristics of Geomaterials, 2008 Atlanta. 629-636.

Diambra, A., Ibraim, E., Wood, D. M. & Russell, A. R. (2010). Fibre reinforced sands: Experiments and modelling. *Geotextiles and Geomembranes,* 28(3), 238-250.

Dos Santos, A. P. S., Consoli, N. C. & Baudet, B. A. (2010). The mechanics of fibre-reinforced sand. *Geotechnique,* 60(10), 791-799.

Gachet, P., Geiser, F., Laloui, L. & Vulliet, L. (2007). Automated digital image processing for volume change measurement in triaxial cells. *Geotechnical Testing Journal, ASTM,* 30(2), 98-103.

Hall, S. A., Bornert, M., Desrues, J., Pannier, Y., Lenoir, N., Viggiani, G. & Besuelle, P. (2010). Discrete and continuum analysis of localised deformation in sand using X-ray mu CT and volumetric digital image correlation. *Geotechnique,* 60(5), 315-322.

Heineck, K. S., Coop, M. R. & Consoli, N. C. (2005). Effect of microreinforcement of soils from very small to large shear strains. *Journal of Geotechnical and Geoenvironmental Engineering, ASCE,* 131(8), 1024-1033.

Ibraim, E. & Fourmont, S. (2007). Behaviour of sand reinforced with fibres. *In:* LING, H. I., CALLISTO, L., LESHCHINSKY, D. & KOSEKI, J., eds. Soil Stress-Stain Behavior: Measurement, Modeling and Analysis, 2007. 807-818.

Indraratna, B., Nimbalkar, S., Christie, D., Rujikiatkamjorn, C. & Vinod, J. (2010). Field Assessment of the Performance of a Ballasted Rail Track with and without Geosynthetics. *Journal of Geotechnical and Geoenvironmental Engineering, ASCE,* 136(7), 907-917.

Ishikawa, T., Sekine, E. & Miura, S. (2011). Cyclic deformation of granular material subjected to moving-wheel loads. *Canadian Geotechnical Journal,* 48(5), 691-703.

Jewell, R. A. & Wroth, C. P. (1987). Direct shear tests on reinforced sand. *Geotechnique,* 37(1), 53-68.

Koike, Y., Nakamura, T., Hayano, K. & Momoya, Y. (2014). Numerical method for evaluating the lateral resistance of sleepers in ballasted tracks. *Soils and Foundations,* 54(3), 502-514.

Le Pen, L., Bhandari, A. & Powrie, W. (2014). Sleeper End Resistance of Ballasted Railway Tracks. *Journal of Geotechnical and Geoenvironmental Engineering, ASCE,* 140(5).

Le Pen, L., Powrie, W., Zervos, A., Ahmed, S. & Aingaran, S. (2013). Dependence of shape on particle size for a crushed rock railway ballast. *Granular Matter,* 15(6), 849-861.

Li, C. & Zornberg, J. G. (2013). Mobilization of Reinforcement Forces in Fiber-Reinforced Soil. *Journal of Geotechnical and Geoenvironmental Engineering, ASCE,* 139(1), 107-115.

Liang, L. Q., Saada, A., Figueroa, J. L. & Cope, C. T. (1997). The use of digital image processing in monitoring shear band development. *Geotechnical Testing Journal, ASTM,* 20(3), 324-339.

Lirer, S., Flora, A. & Consoli, N. C. (2011). On the strength of fibre-reinforced soils. *Soils and Foundations,* 51(4), 601-609.

Macari, E. J., Parker, J. K. & Costes, N. C. (1997). Measurement of volume changes in triaxial tests using digital imaging techniques. *Geotechnical Testing Journal, ASTM,* 20(1), 103-109.

Mcdowell, G. R., Harireche, O., Konietzky, H., Brown, S. F. & Thom, N. H. (2006). Discrete element modelling of geogrid-reinforced aggregates. *Proceedings of the Institution of Civil Engineers-Geotechnical Engineering,* 159(1), 35-48.

Michalowski, R. L. & Cermak, J. (2002). Strength anisotropy of fiber-reinforced sand. *Computers and Geotechnics,* 29(4), 279-299.

Michalowski, R. L. & Cermak, J. (2003). Triaxial compression of sand reinforced with fibers. *Journal of Geotechnical and Geoenvironmental Engineering, ASCE,* 129(2), 125-136.

Michalowski, R. L. & Zhao, A. G. (1996). Failure of fiber-reinforced granular soils. *Journal of Geotechnical Engineering, ASCE,* 122(3), 226-234.

Rechenmacher, A. L. (2006). Grain-scale processes governing shear band initiation and evolution in sands. *Journal of the Mechanics and Physics of Solids,* 54(1), 22-45.

Rechenmacher, A. L. & Finno, R. J. (2004). Digital image correlation to evaluate shear banding in dilative sands. *Geotechnical Testing Journal, ASTM,* 27(1), 13-22.

Schofield, A. N. & Wroth, P. (1968). *Critical state soil mechanics*, McGraw-Hill.

Sevi, A. & Ge, L. (2012). Cyclic Behaviors of Railroad Ballast within the Parallel Gradation Scaling Framework. *Journal of Materials in Civil Engineering,* 24(7), 797-804.

Sevi, A. F. (2008). *Physical modeling of railroad ballast using the parallel gradation scaling technique within the cyclical triaxial framework.* PhD Thesis, Missouri Univ. of Science and Technology, Rolla, MO.

Sevi, A. F., Ge, L. & Take, W. A. (2009). A Large-Scale Triaxial Apparatus for Prototype Railroad Ballast Testing. *Geotechnical Testing Journal, ASTM,* 32(4), 297-304.

White, D. J., Take, W. A. & Bolton, M. D. (2003). Soil deformation measurement using particle image velocimetry (PIV) and photogrammetry. *Geotechnique,* 53(7), 619-631.

## List of symbols

$A_f$ - total cross sectional area of fibre per unit volume of grains

$A_g$ - area of grains

$A_\alpha$, $B_\alpha$ - constants for a given combination of granular material, fibre type, fibre geometry and fibre content

$d$ - rate of dilation

$D_{50}$ - mean grain size

$e$ - void ratio

$E_f$ - fibre Young's modulus

$I_D$ - density index

$L_f$ - fibre length

$L_N$ - normalized length

$p$ - mean effective stress

$p''$ - corrected mean effective stress

$q$ - deviator stress

$q''$ - corrected deviator stress

$v$ - specific volume

$V_f$ - volume of fibres

$V_{fr}$ - volumetric fibre ratio

$V_s$ - volume of the grains (or "solids")

$V_v$ - volume of voids

$W_f$ - fibre width

$W_N$ - normalized width

$\alpha$ - fibre/grain interaction factor

$\beta$ - average orientation of the fibres

$\varepsilon_a$ - axial strain

$\varepsilon_r$ - radial strain

$\varepsilon_{vol}$ - volumetric strain

$\varepsilon_\gamma$ - triaxial shear strain

$\eta$ - stress ratio

$\eta''$ - corrected stress ratio

$\sigma'_3$ - radial stress

$\sigma''_3$ - corrected lateral stress

$\sigma'_f$ - additional lateral stress

# Tables

Table 1. Typical values of the basic properties of polyethylene fibres

| | Polyethylene |
|---|---|
| Specific gravity | 0.92 |
| Tensile strength | 20.3 MPa[1]; 11.2 MPa[2] |
| Elastic modulus | 0.38 GPa |
| Softening temperature | 85°C |
| Moisture absorption | < 0.1% |

[1] Longitudinal; [2] Transverse

Table 2. Median grain size, fibre volume fraction, initial void ratios and relative density indices, and actual and normalised fibre dimensions for the $^1/_3$ and $^1/_5$ SB specimens

| Granular medium | $D_{50}$ (mm) | $V_{fr}$ (%) | $e_o$ | $I_D$ | $L_f$ (mm) | $W_f$ (mm) | $L_N$ | $W_N$ |
|---|---|---|---|---|---|---|---|---|
| $^1/_5$ SB | 8 | - | 0.89[1] | 0.03 | - | - | | |
| | | - | 0.83[2] | 0.45 | - | - | | |
| | | - | 0.74[3] | 0.99 | - | - | | |
| | | 1.6 | 0.83 | 0.43 | 58 | 20 | 7.1 | 2.5 |
| | | 3.2 | 0.88 | 0.12 | 58 | 20 | 7.1 | 2.5 |
| | | 6.5 | 0.97 | -0.44 | 58 | 20 | 7.1 | 2.5 |
| $^1/_3$ SB | 14 | - | 0.87[1] | 0.21 | - | - | | |
| | | - | 0.76[3] | 0.87 | - | - | | |
| | | 1.6 | 0.79 | 0.69 | 100 | 35 | 7.1 | 2.5 |
| | | 3.2 | 0.91 | -0.04 | 100 | 35 | 7.1 | 2.5 |

Table 3. Summary of image capture system characteristics

| | |
|---|---|
| Image aspect ratio | 3V:2H |
| Focus mode | Manual |
| Camera calibration | Camera Calibration Toolbox for MATLAB (Bouguet, 2008), with a planar checkerboard calibration pattern at different orientations about the image plane position, keeping the camera stationary |
| Principal point | Assumed to be at the image centre |
| Lens distortion | Insignificant |
| Interpolation function | Bi-cubic, evaluated at 1/100 pixel intervals giving a sub-pixel resolution of 0.01 pixel |
| Precision | Better than 0.0033 pixel for the 181 × 181 pixel subset used for image analysis, based on the empirical equation given by White et al. (2003) |
| Accuracy | Better than 0.10 pixels or 0.004 mm in the object-space at an image scale of 0.04 mm/pixel at the centre of the image (Bhandari et al. (2012) |

Table 4. Fibre/grain interaction factors for each specimen

| Granular medium | $D_{50}$ (mm) | $V_{fr}$ (%) | $e_o$ | $\eta$ | $\eta''$ | $A_\alpha$ | $B_\alpha$ | $\alpha$ | $\sigma_f$ at $d = 0$ (kPa) |
|---|---|---|---|---|---|---|---|---|---|
| $^1/_5$ SB | 8 | loose | 0.89 | 1.565 | - | - | - | - | - |
| | | Med. dense | 0.83 | 1.570 | - | - | - | - | - |
| | | Dense | 0.74 | 1.625 | - | - | - | - | - |
| | | 1.6 | 0.83 | 1.710 | 1.588 | 0.166 | -0.6 | 0.302 | 3.8 |
| | | 3.2 | 0.88 | 1.834 | 1.587 | 0.158 | -0.6 | 0.184 | 8.8 |
| | | 6.5 | 0.97 | 2.143 | 1.585 | 0.179 | -0.6 | 0.129 | 26.2 |
| $^1/_3$ SB | 14 | - | 0.87[1] | 1.588 | - | - | - | - | - |
| | | - | 0.76[3] | 1.602 | - | - | - | - | - |
| | | 1.6 | 0.79 | 1.747 | 1.587 | 0.220 | -0.4 | 0.270 | 5.5 |
| | | 3.2 | 0.91 | 1.945 | 1.585 | 0.147 | -0.4 | 0.125 | 13.4 |

# Figures

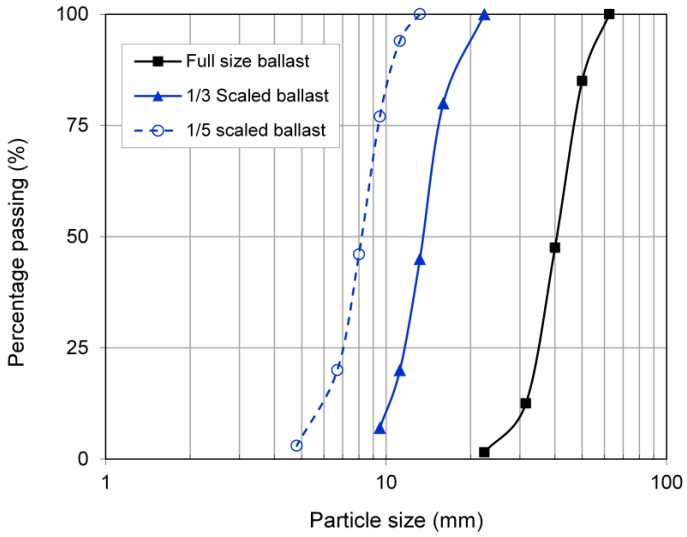


Figure 1. Grain size distribution of 1/5th and 1/3rd scaled, and full size ballast (Network Rail specification)

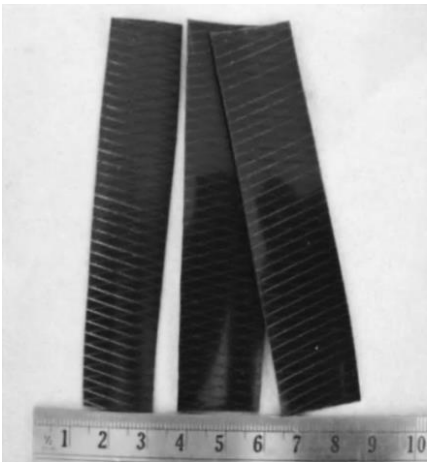


Figure 2. Polyethylene fibres (or strips) used in the triaxial tests

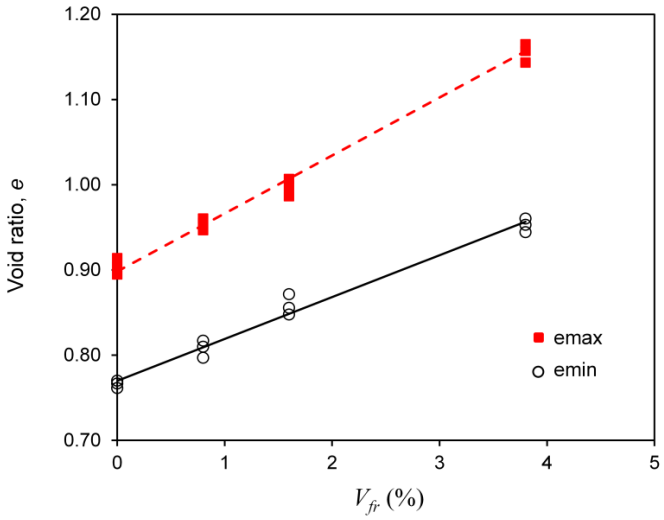


Figure 3. Effect of increasing $V_{fr}$ on the maximum and minimum void ratios of fibre reinforced $^1/_3$ SB achievable using a given compactive effort

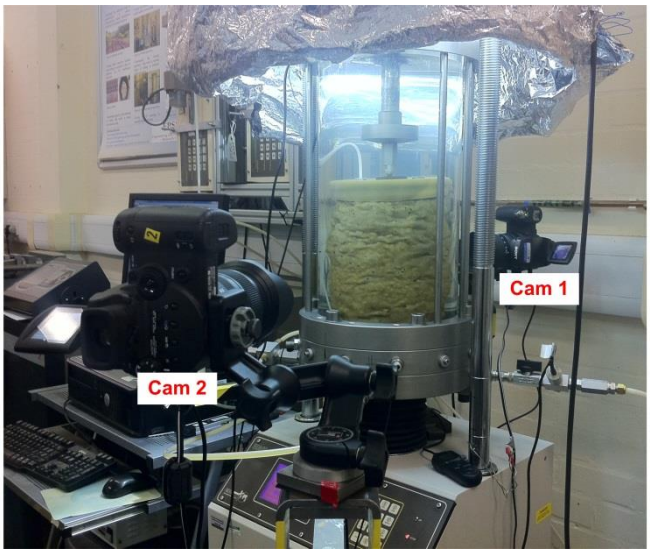


Figure 4. The triaxial setup for image-based deformation studies showing a triaxial specimen in the transparent cell during shear, cameras positioned at angular distance of ~120°, uniform light source and light reflecting curtain (which is in a raised position in this image)

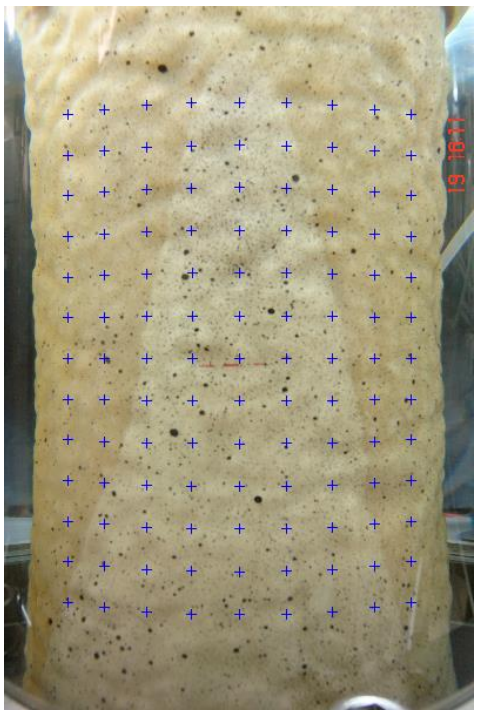

Figure 5. Typical image of a triaxial specimen captured during shear, showing grids used for image-based deformation measurement and the speckled pattern on the membrane

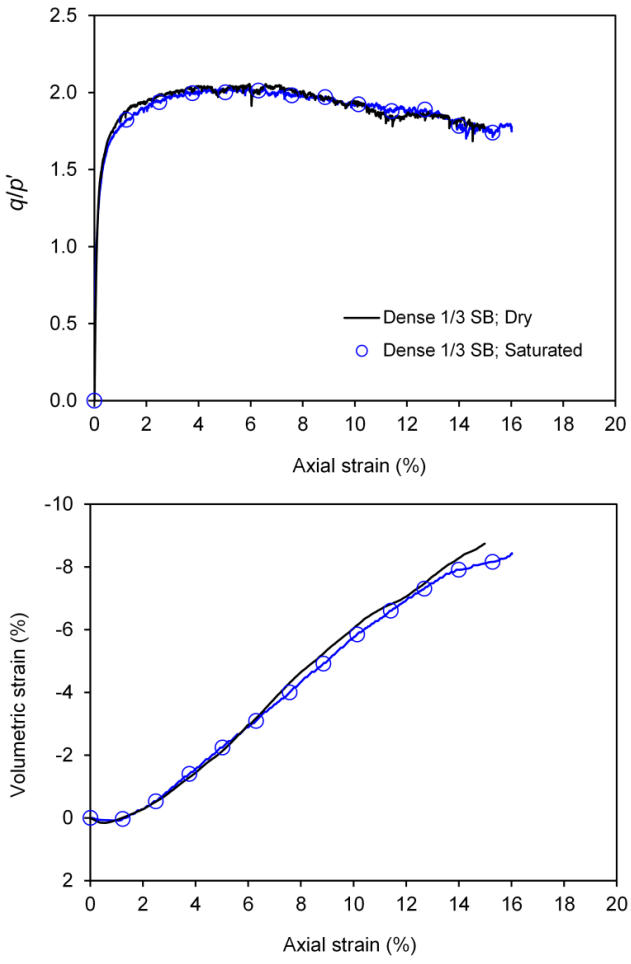


Figure 6. Comparison of triaxial tests carried out on dry and saturated unreinforced $^{1}/_{3}$ SB specimens at an effective stress of 30 kPa. Volumetric strains in the test on the dry specimen test were measured using the cell pressure controller, and in the test on the saturated specimen using the pore pressure controller

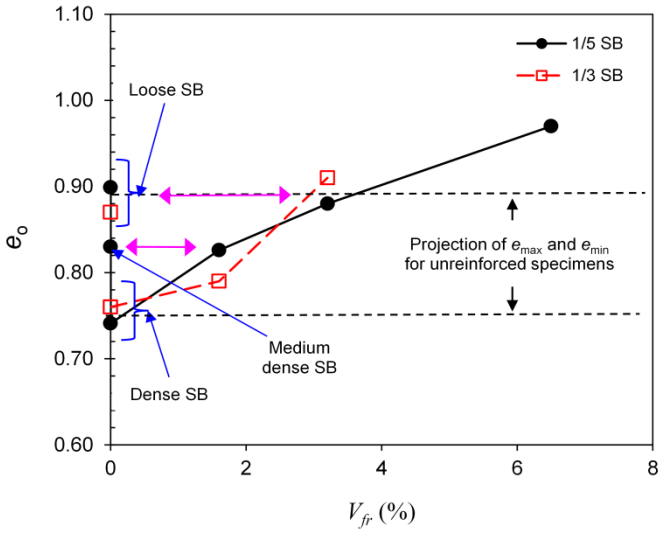


Figure 7. Initial void ratios, $e_o$, of triaxial specimens shown as a function of the fibre to solids ratio, $V_{fr}$

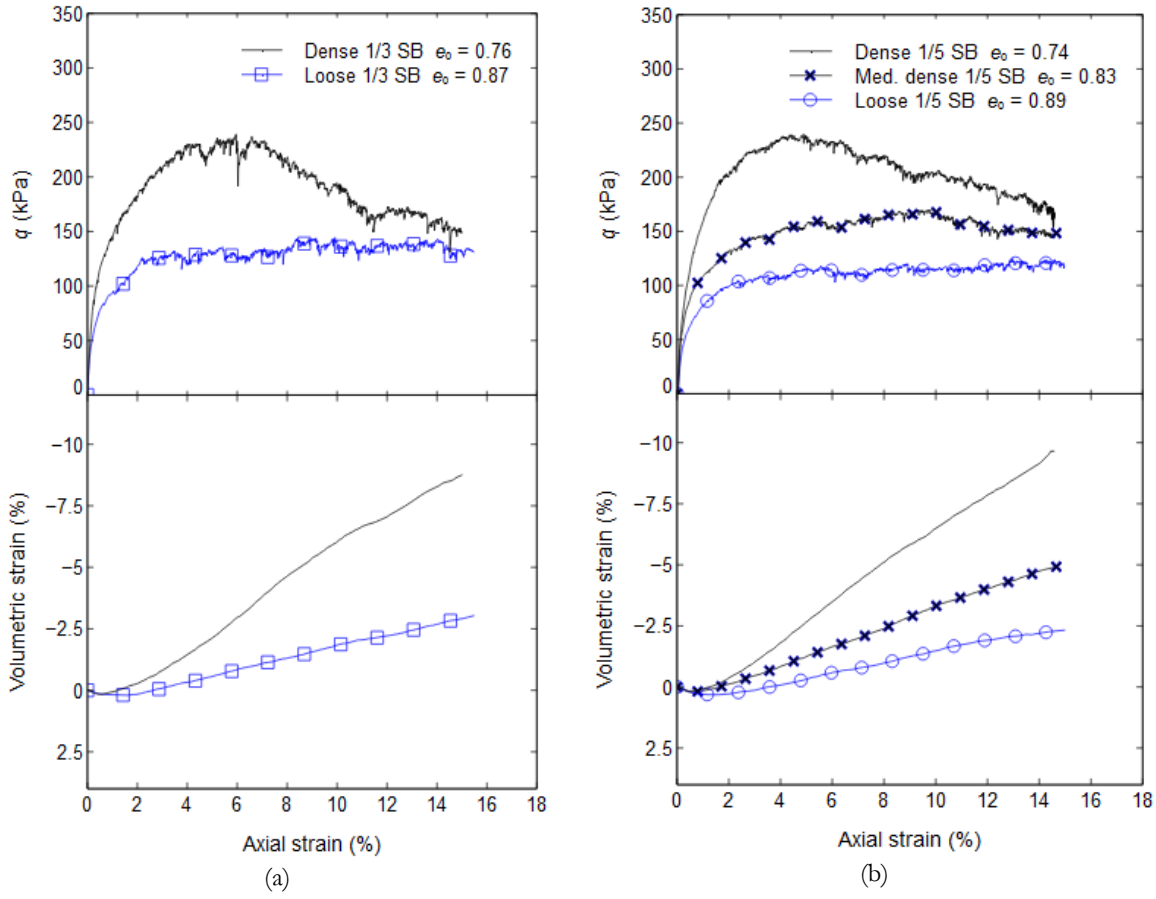


Figure 8. Deviator stress, $q = (\sigma_a - \sigma_r)$, and volumetric strain plotted against axial strain for unreinforced specimens of (a) $^1/_3$ and (b) $^1/_5$ SB at different initial densities. Cell pressure = 30 kPa

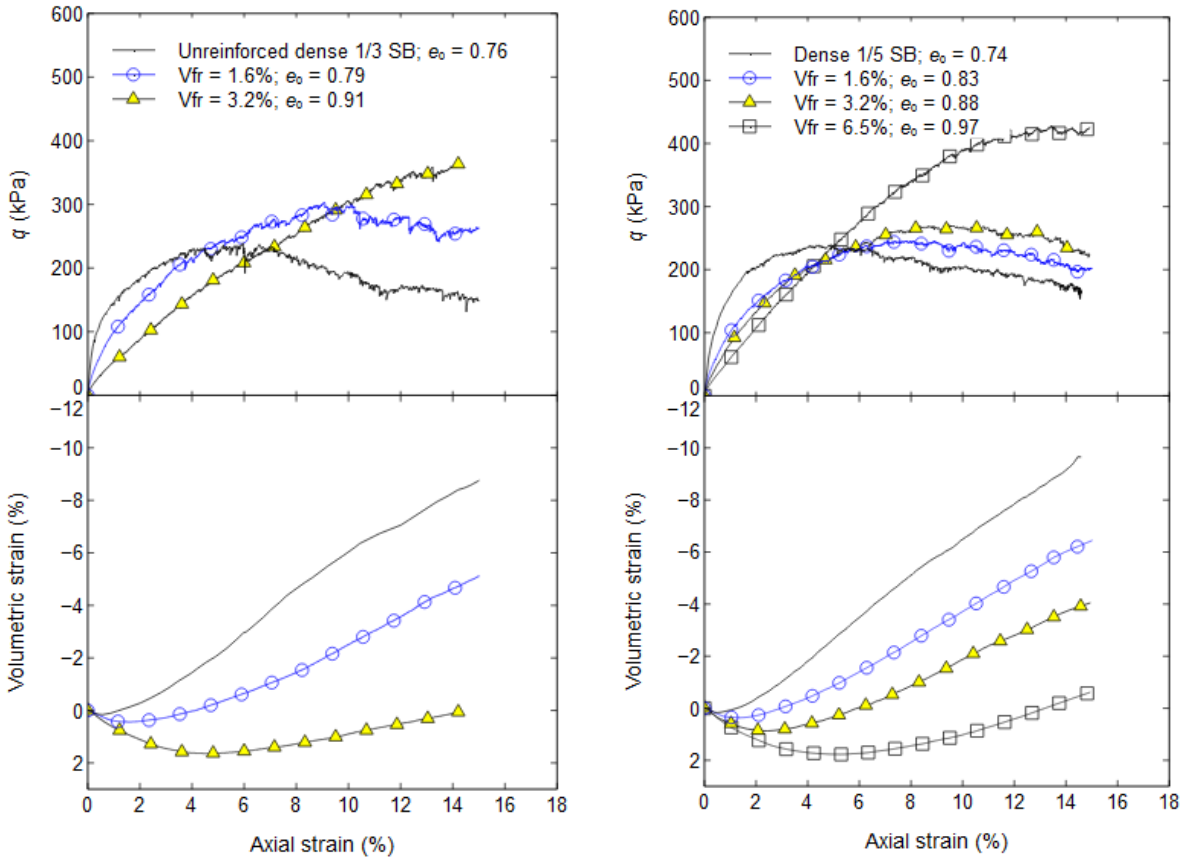


Figure 9. Conventional deviator stress, $q = (\sigma_a - \sigma_r)$, and volumetric strain plotted against axial strain for unreinforced specimens of (a) $^1/_3$ and (b) $^1/_5$ reinforced SB with different fibre contents. Cell pressure = 30 kPa

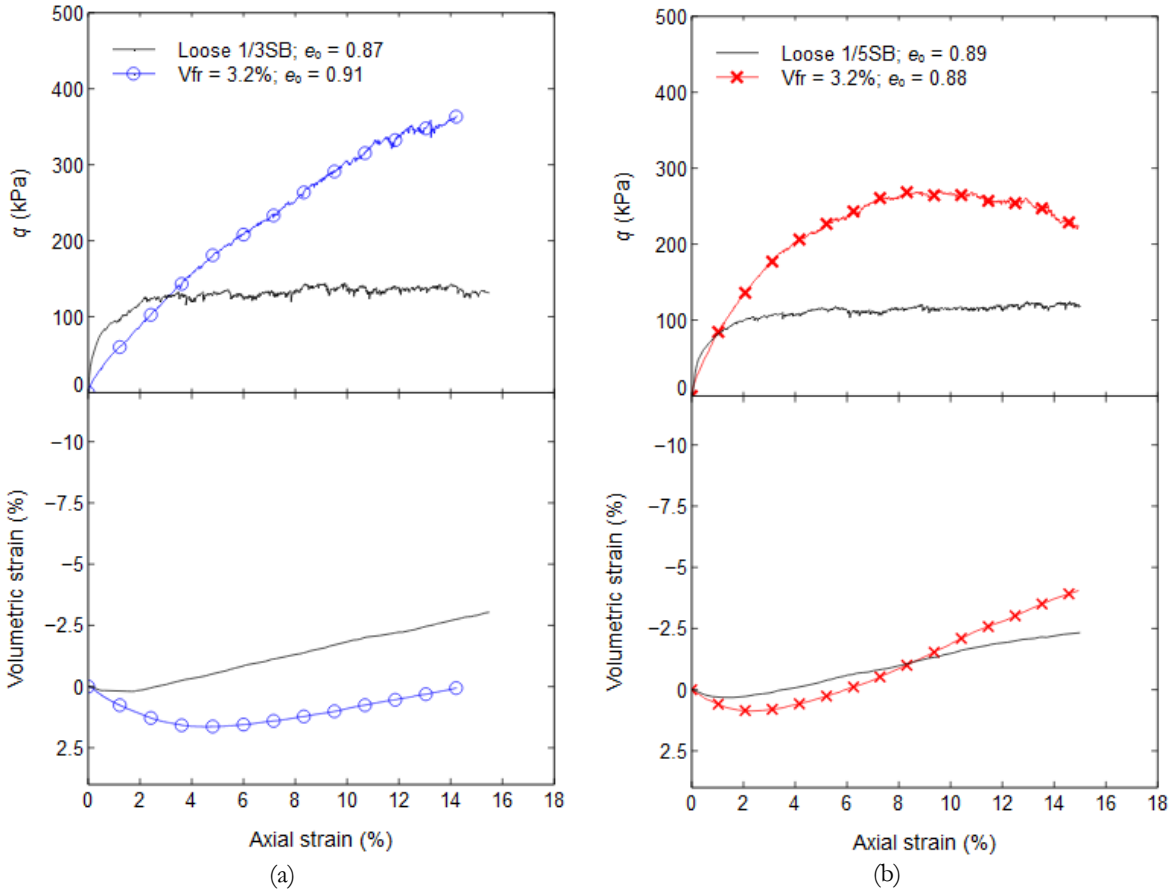


Figure 10. Conventional deviator stress, $q = (\sigma_a - \sigma_r)$, and volumetric strain plotted against axial strain for reinforced and unreinforced specimens of (a) and (c) 1/3 and (b) and (d) $^1/_5$ SB having approximately the same initial void ratio $e_o$. Cell pressure = 30 kPa (a) dense $^1/_3$ SB ($e_o$ = 0.76) and $V_{fr}$ = 1.6 % ($e_o$ = 0.79); (b) medium $^1/_5$ SB ($e_o$ = 0.83) and $V_{fr}$ = 1.6% ($e_o$ = 0.83); (c) loose $^1/_3$ SB ($e_o$ = 0.87) and $V_{fr}$ = 3.2 % ($e_o$ = 0.91); (d) loose $^1/_5$ SB ($e_o$ = 0.89) and $V_{fr}$ = 3.2 % ($e_o$ = 0.88)

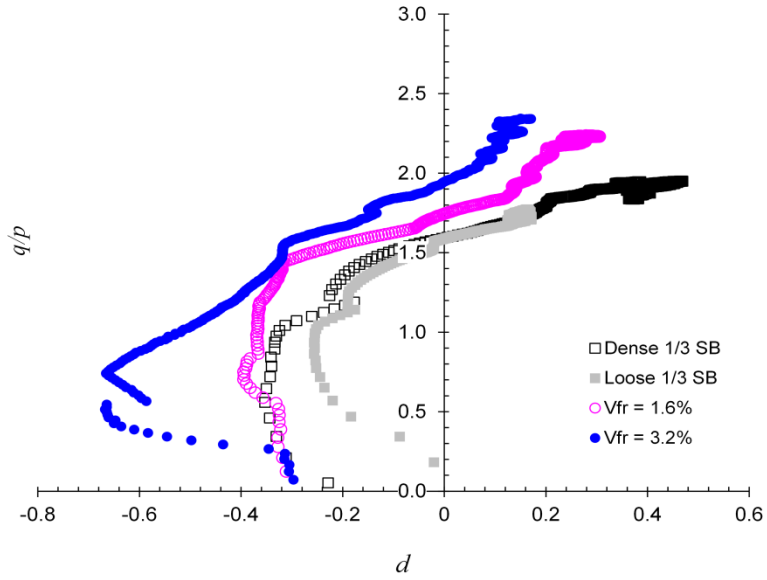


Figure 11. Stress ratio, $q/p$, plotted against rate of dilation, $d$, for unreinforced $^1/_3$ SB at different initial densities and reinforced $^1/_3$ SB at different $V_{fr}$ values

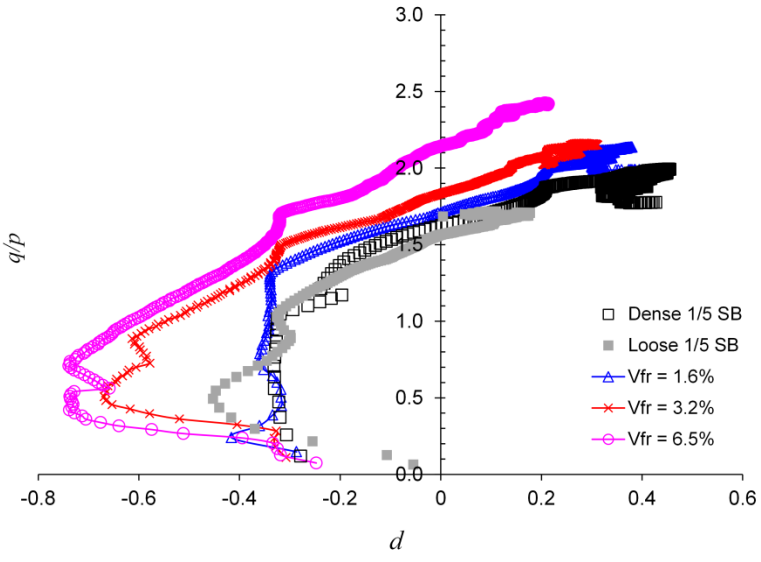


Figure 12. Stress ratio, $q/p$, plotted against rate of dilation, $d$, for unreinforced $^1/_5$ SB at different initial densities and reinforced $^1/_5$ SB with different fibre contents $V_{fr}$

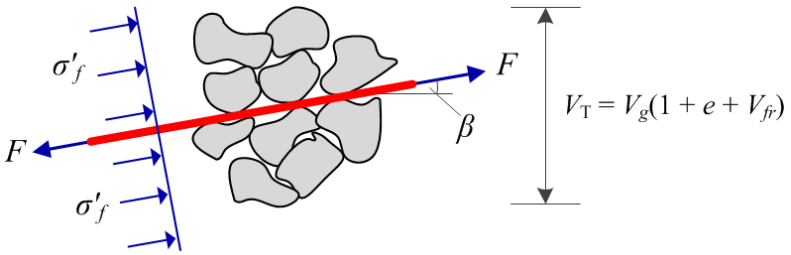


Figure 13. Illustration of the concept of additional apparent confinement of gravel due to tensile force from fibres on fibre-grain interaction

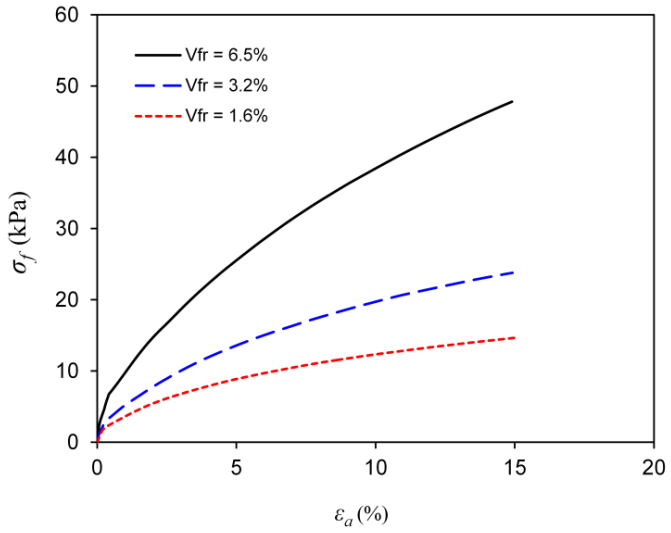


Figure 14. Evolution of additional effective lateral stress, $\sigma'_f$, with axial strain for reinforced $^1/_5$ SB specimens

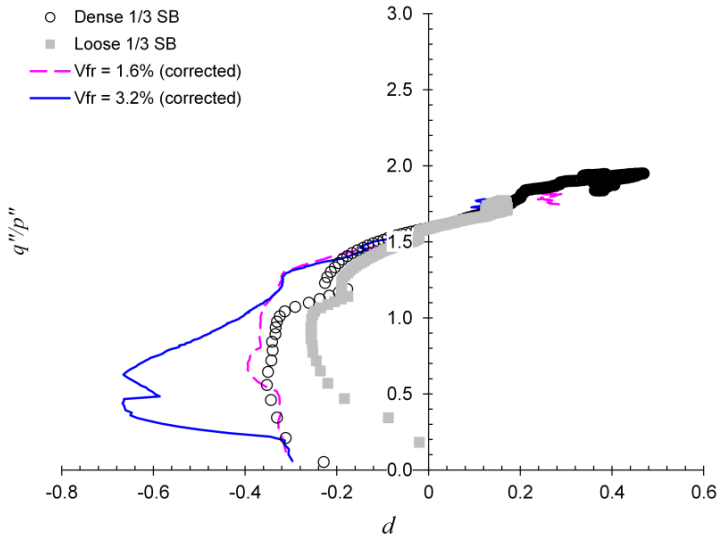


(a)

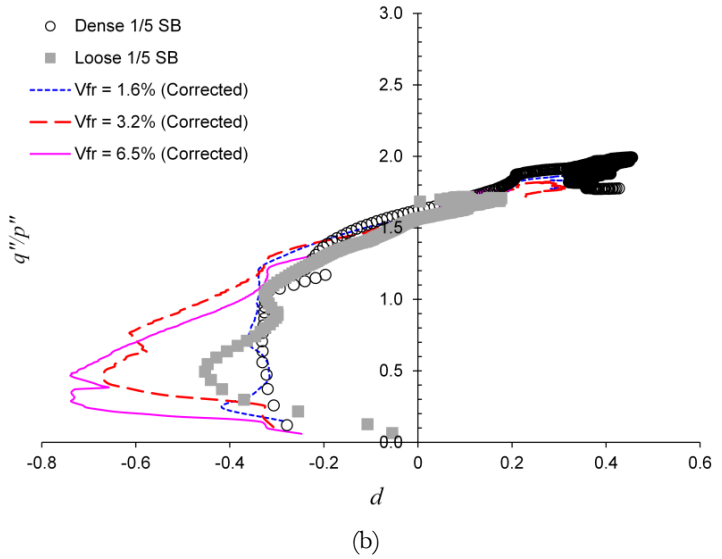


(b)

Figure 15. Corrected stress ratio, *q"/p"*, plotted against rate of dilation, *d*, for (a) $^{1}/_{3}$ SB specimens (b) $^{1}/_{5}$ SB specimens

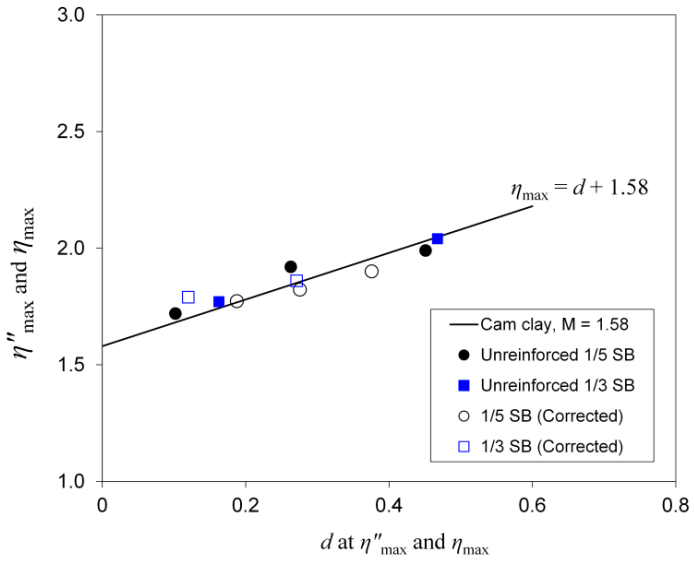


Figure 16. Rate of dilation, $d_{max}$, at maximum corrected stress ratio, $\eta''_{max}$, for all fibre reinforced and unreinforced scaled ballast specimens at a cell pressure of 30 kPa

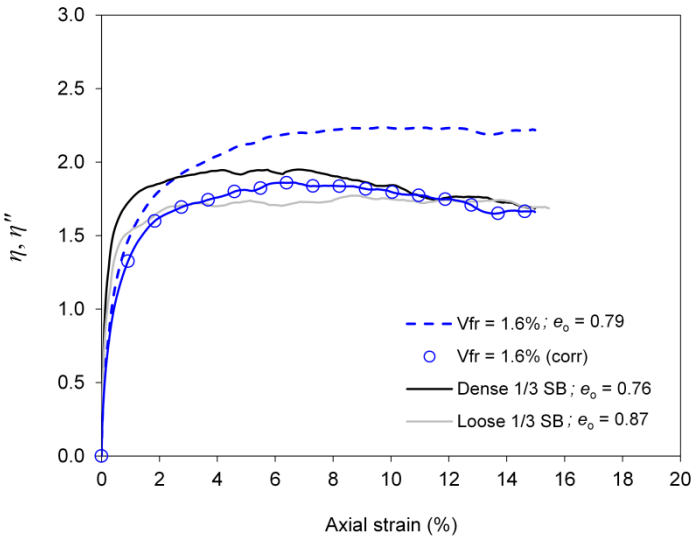


(a)

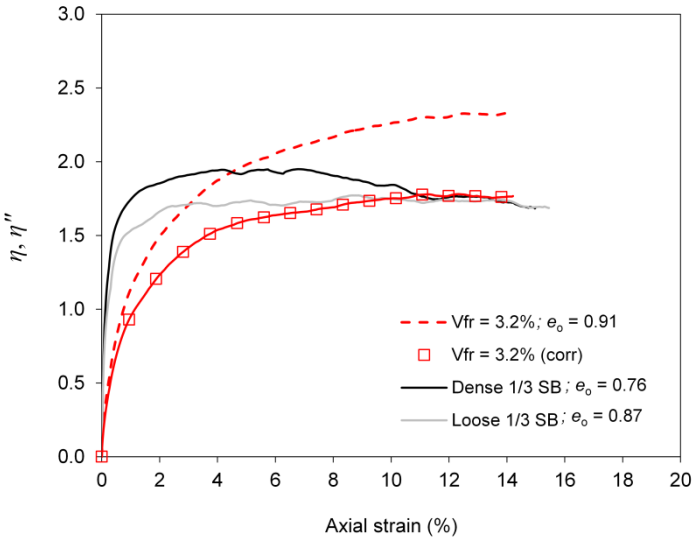


(b)

Figure 17. Stress ratio (corrected and uncorrected) against axial strain for reinforced $^1/_3$ SB (a) $V_{fr}$ = 1.6 % (b) $V_{fr}$ = 3.2 %

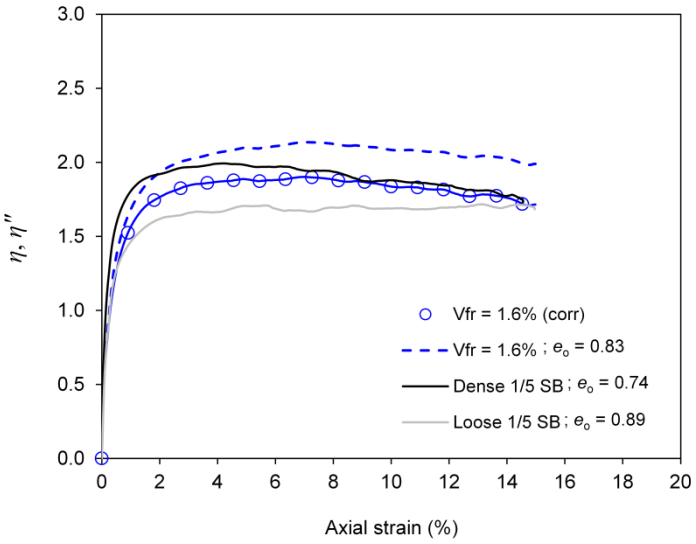


(a)

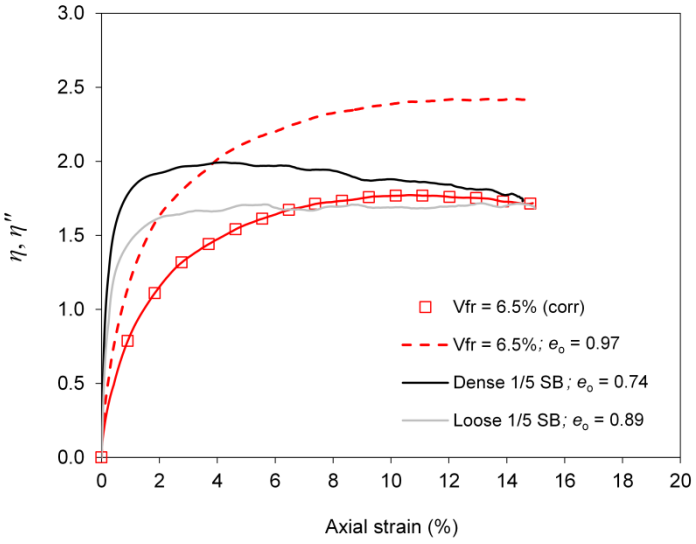


(b)

Figure 18. Stress ratio (corrected and uncorrected) against axial strain for reinforced $^1/_5$ SB (a) $V_{fr}$ = 1.6 % (b) $V_{fr}$ = 6.5 %

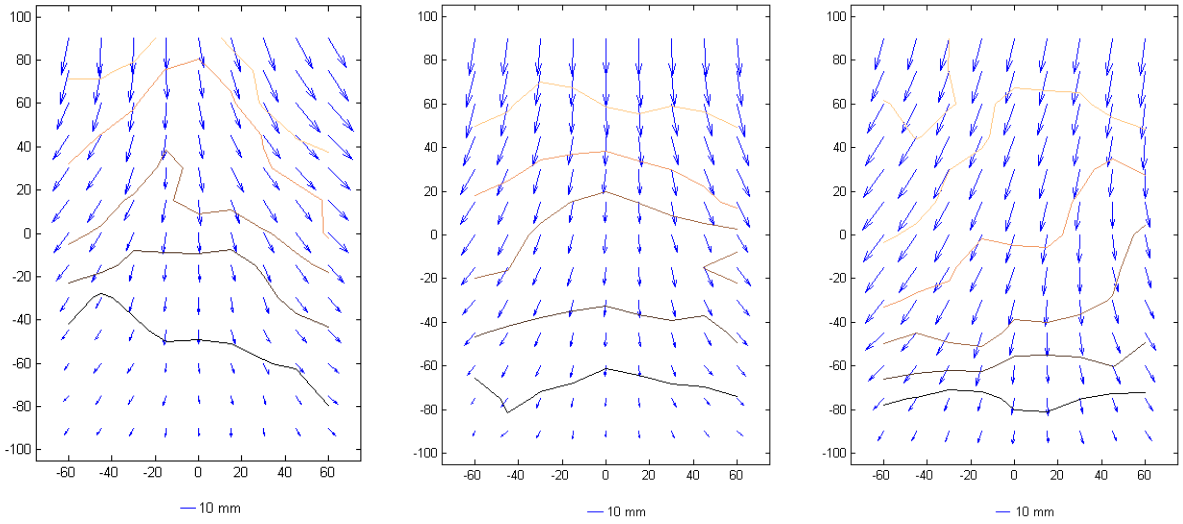


(a) Dense SB (b) Medium dense SB (c) Loose SB

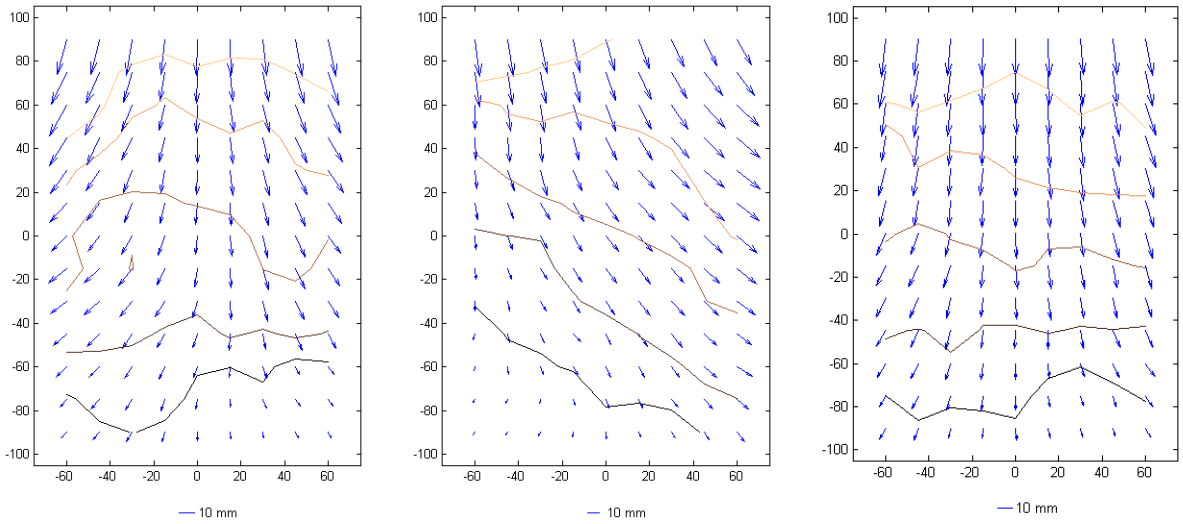


(d) $V_{fr}$ = 1.6 % (e) $V_{fr}$ = 3.2 % (f) $V_{fr}$ = 6.5 %

Figure 19. Cumulative displacement vectors over an axial strain range of 0.25 – 10.25 % for (a) dense (b) medium dense and (c) loose specimens of unreinforced $^1/_5$ SB, and reinforced specimens with volumetric fibre ratios $V_{fr}$ of (d) $V_{fr}$ = 1.6 % (e) $V_{fr}$ = 3.2 % and (f) $V_{fr}$ = 6.5 %

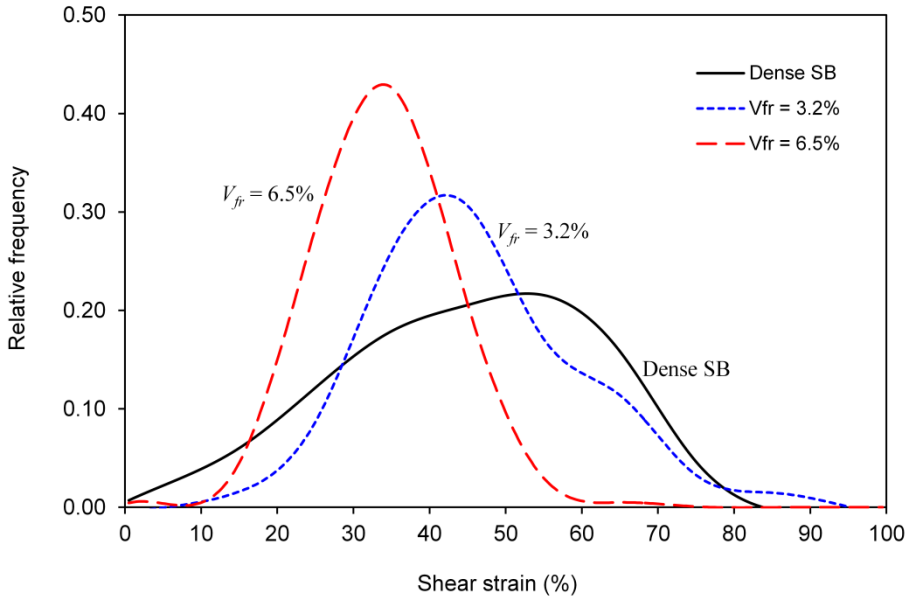


Figure 20. Trend lines of relative frequency of the measured local maximum shear strains for a global cumulative axial strain range of 10 %; dense specimens of $^1/_5$ SB having different degrees of fibre reinforcement but similar density index, $I_D$,: dense unreinforced $^1/_5$ SB ($e_o$ = 0.74, $I_D$ = 0.99), reinforced $^1/_5$ SB having $V_{fr}$ = 3.2 % ($e_o$ = 0.88, $I_D$ = 0.96), and reinforced $^1/_5$ SB having $V_{fr}$ = 6.5 % ($e_o$ = 0.97, $I_D$ = 0.99)